Eur. J. Mech. A/Solids 19 (2000) 259–275

S0997-7538(99)00164-3/FLA

On the mechanics of braided composites in tension

Anne-Marie Harte, Norman A. Fleck

Cambridge Centre for Micromechanics, Cambridge University Engineering Dept., Trumpington Street, Cambridge, CB2 1PZ, UK

(Received 28 May 1999; revised and accepted 29 November 1999)

Abstract – An experimental investigation is reported on the uniaxial tensile behaviour of braided tubes, comprising glass fibres in an epoxy matrix. The failure mode switches from fibre fracture to neck propagation when the helix angle, defined as the angle between the fibre direction and the axis of the tube, exceeds about 45°. The observed neck geometry is used to deduce the evolution of deformation and damage within the matrix, and a work calculation is used to estimate the steady state neck propagation stress from a micromechanical model of braid deformation. A failure chart is constructed to show the effect of braid geometry on elastic modulus, yield strength, strain to failure and energy absorption of the braid. © 2000 Éditions scientifiques et médicales Elsevier SAS

braided composite / constitutive equation / tension

1. Introduction

Traditional fibre composites are fabricated by laying up pre-impregnated plies of aligned fibres. In this way the strength and stiffness of the composite can be tailored in given directions. However, laminated composites have relatively low toughness against in-plane splitting and suffer from delamination between plies. Textile composites are different. They are manufactured by fabrication methods derived from the textile industry: weaving, knitting, stitching and braiding. The inter-lacing of the tows in the through-thickness direction increases the splitting toughness and largely eliminates the delamination problem. Additionally, braided composites can be fabricated directly into net shape, decreasing the manufacturing time and cost compared with laminates.

This paper focuses on braided textile composites. The bundles of fibres, or tows, in a braid are interlaced in the same way that the ribbons in the Maypole dance are interlaced. The result is a woven tubular structure. We shall consider a regular braid comprised of two sets of tows oriented at helix angles of $\pm\theta$ to the axial direction; the helix angle θ is defined as the angle between the tow direction and the axis of the tube as shown in *figure 1*. When such a braid is stretched axially, the mechanism of deformation is predominantly shear of the matrix parallel to each tow.

Much effort has been spent in modelling the elastic bulk properties of woven and braided composites using laminate plate theory (Chou, 1992) but comparatively little work has been done in understanding the micromechanics of deformation. Here, we examine the tensile deformation and fracture responses of a regular glass fibre braid without a matrix and with a toughened epoxy matrix. The mechanical response of the dry braid (containing no matrix) is examined in order to develop an understanding of the kinematics of braid deformation. The toughened epoxy matrix is representative of a typical polymer matrix for engineering use.

The structure of the paper is as follows. First, tensile tests are reported for single-layer $\pm\theta$ tubular braids constructed from E-glass fibres with an epoxy matrix. The helix angle θ is the dominant geometrical parameter of interest and strongly influences the modes of deformation and failure. Second, a failure chart is constructed

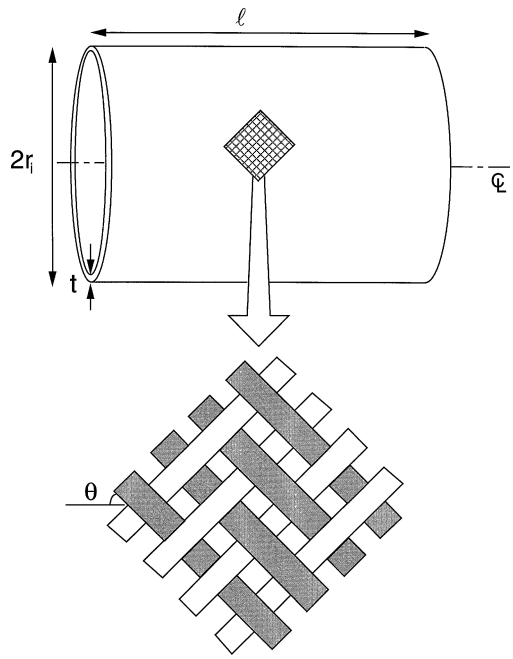

Figure 1. Sketch of a braided cylinder with the 'two-over-two-under' unit cell of a regular braid.

which shows the effect of helix angle on the effective axial properties of the braid such as elastic modulus, yield strength, strain to failure and the amount of energy absorbed to failure. Third, the neck geometry in steady-state neck propagation is examined and is used to motivate a constitutive model for the braid. The constitutive model is used in an energy balance calculation to predict the tensile load required for steady-state neck propagation in braids with helix angles greater than 45°. The steady state propagation of instabilities has been observed in many material systems, including the buckling of underwater pipelines (Kyriakides and Chang, 1990; Kyriakides, 1994), the cold drawing of polymers and the inflation of long cylindrical balloons (Chater and Hutchinson, 1984a, b). The propagation load can be estimated in all of these cases by an energy balance. This technique is used herein to predict the steady state neck propagation stress.

2. Experimental investigation of the tensile response of braided tubes

A hand braiding machine was used to manufacture circular tubes of 2-harness regular braid from E-glass fibre tows. Each tow was a bundle of 1600 untwisted glass fibres of individual diameter 18.9 μm. The braided tubes (with dimensions given in *table I*) comprised a single layer of $\pm\theta$ braid, with 32 tows in each of the $+\theta$ and $-\theta$ directions, as sketched in *figure 1*. Specimens were manufactured with a uniform braid angle in the range 23° to 55° by placing the braids on circular cylindrical mandrels of various diameter; after application of the matrix the glass fibre volume fraction was 40% independent of the initial helix angle.

The epoxy matrix employed was a two part toughened casting epoxy, known as Araldite MY 753 and hardener HY 956, supplied by Ciba-Geigy. It was hand-brushed onto the dry braid in order to impregnate the tows, and the specimens were cured in an air oven at 100 C for 20 minutes.

Table I. Geometry of braided tubes used for tensile tests.

Helix angle θ_0	Wall thickness t (mm)	Diameter $2r$ (mm)	Gauge length ℓ (mm)
23°	1.2	25.37	69
40°	0.98	42.20	188
45°	0.95	46.2	200
55°	0.93	53.0	280
40° no matrix	0.95	42.20	108

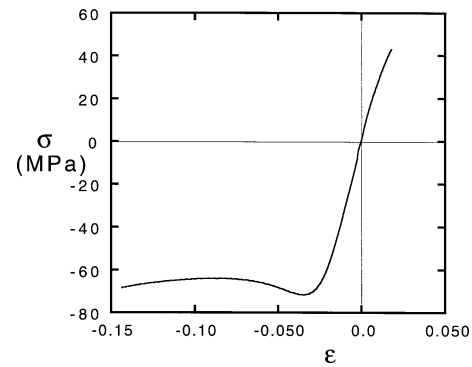

Figure 2. Nominal stress versus nominal strain uniaxial response of the epoxy matrix.

2.1. Preliminary tests on the fibres and matrix

Preliminary uniaxial tension tests revealed that the glass fibres behave in a linear elastic manner with a Young's modulus of 63 GPa and a tensile strength of 1.9 GPa. The uniaxial response of a bulk sample of the epoxy is shown in *figure 2*, for a nominal strain rate of 10^{-3} s^{-1}. The Young's modulus is 2.8 MPa, the tensile strength is 43 MPa and the compressive strength is 72 MPa. The observed behaviour is brittle in tension but ductile in compression due to shear yielding.

2.2. Tensile tests

The tensile behaviour of the regular braids was measured for two different matrices: no matrix (a 'dry braid') and the epoxy matrix. The specimens were tested in uniaxial tension at a strain rate of 3×10^{-4} s^{-1}, for four initial helix angles $\theta_0 = 23°$, 40°, 45° and 55°.

The nominal axial strain in the tensile specimens was measured by several methods. The braids with small helix angles ($\theta_0 = 23°$) failed at low strains (less than 3%) and strain gauges were used to measure the axial strain. For braids of intermediate angles ($\theta_0 = 40°$ and 45°) the strain magnitude exceeded the capacity of strain gauges, and a clip-gauge was employed. For the braids of largest helix angle ($\theta = 55°$), the diameter decreased substantially as the braids stretched by a nominal strain of up to 60%. Attempts to fasten clip gauges onto the surface by elastic bands around the circumference of the sample failed, as did attempts to clip the gauges onto metal tabs adhered to the surface. Instead, a clip gauge of strain capacity 60% was adhered to rubber tabs on the surface of the specimen. These tabs of dimension 10 mm × 10 mm × 1 mm were adhered to the surface of the braids using Prism 480 Rubber Toughened Locktite adhesive; the tabs could accommodate the motion of the

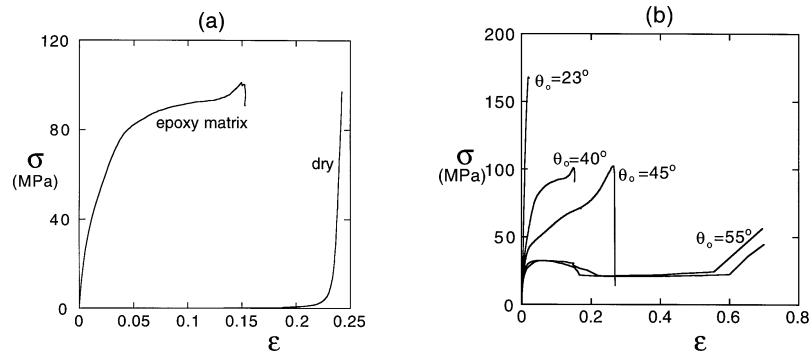

Figure 3. (a) The tensile nominal stress–strain behaviour of a dry braid and of an epoxy-matrix braid, for a helix angle $\theta_0 = 40°$; (b) The nominal stress–strain behaviour of glass fibre-epoxy braids, with initial helix angles $\theta_0 = 23°$, 40°, 45° and 55°.

tows in the braid without debonding from the tubes. The tests on the large angle specimens were videotaped, and nominal axial strains measured from the video recording compared well with those measured by the clip gauge. Strains in excess of 60% were also measured from the video recordings.

Additionally, the nominal strain along the local fibre direction was measured by adhering strain gauges of 1 mm gauge length to an individual tow before the braid was cast in epoxy.

2.3. Results of tensile tests on braids

The results of the tensile tests are presented primarily in the form of the nominal axial stress on the tube wall σ versus the nominal axial strain ε. The contribution of the epoxy matrix to the tensile response of the braided tube is shown in *figure 3a* for the case $\theta_0 = 40°$: the tensile response is given both for a dry braid and for an epoxy-matrix braid.

The dry braid carries negligible axial stress (less than 0.1 MPa) at axial strains less than the lock-up strain of about 0.22, see *figure 3a*: the fibres scissor over each other resisted only by friction. When the nominal axial strain equals about 0.22, the tows become close-packed and there is a sharp up-turn in the axial stress. In contrast, the glass fibre-epoxy braid strain hardens rapidly to a peak strength of about 100 MPa at a failure strain of 0.15; the reduced failure strain reflects the fact that the epoxy matrix prevents the fibres from becoming close-packed.

The effect of the initial helix angle θ_0 on the tensile response is shown in *figure 3b* for the epoxy-matrix braid. The shape of the stress–strain curve is highly sensitive to the magnitude of θ_0, and results are shown for $\theta_0 = 23°$, 40°, 45° and 55°. Repeat tests show that the scatter in strength from test to test is small; for example, repeat tests for $\theta_0 = 55°$ are included in *figure 3b*.

Consider first a braid of initial helix angle $\theta_0 = 23°$. The axial stiffness is 9.42 GPa, the failure strength is 167 MPa and the failure strain is 0.022. It is clear from *figure 3b* that the response is almost linear elastic to fracture.

Second, consider a braid of intermediate helix angle ($\theta = 40°$), as shown in *figure 3b*. The epoxy begins to microcrack at an axial strain of 0.03; the microcracking is visible as whitening and first occurs at the cross-over points of the tows. As the specimen elongates, the fibres continue to scissor and microcracking within the matrix spreads until it envelops the entire microstructure at an axial strain level of about 0.1. At the macroscopic level, axial extension of the tube occurs without necking and catastrophic failure is by fibre fracture. The measured

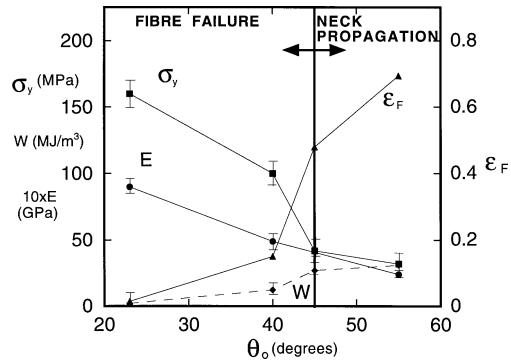

Figure 4. Failure chart for braided tubes in tension. The nominal yield strength σ_y, nominal strain to failure ε_F, specific energy absorbed W, and initial modulus E are each plotted against the initial helix angle θ_0. The competing modes are fibre failure and neck propagation.

axial modulus of the tube wall is 5.0 GPa, the 2% offset yield strength is 72 MPa and the nominal failure strain is 0.15.

Third, consider a braid of large helix angle ($\theta = 55°$). The stress–strain curve is almost linear up to an axial strain of 0.02. The nominal stress-nominal strain response becomes increasingly nonlinear and reaches a local maximum, associated with neck formation. Once the neck has fully formed it propagates axially at constant load. Plastic deformation of the necked material is accompanied by microcracking. Steady-state neck propagation is associated with a long plateau in the nominal stress versus nominal strain curve. After the entire specimen has necked, the stress–strain curve rises and fibre fracture ensues. The initial elastic stiffness is 2.2 GPa, the 2% offset yield strength is 30 MPa, the plateau stress is 21 MPa and the nominal failure strain is 0.7. The final helix angle at specimen fracture θ_L is 21° for all three values of initial helix angle θ_0.

The tensile behaviour of regular glass-epoxy braids is summarised in *figure 4*. The nominal yield strength σ_y, nominal strain to failure ε_F, specific energy absorbed W, and initial modulus E are each plotted against the initial helix angle, θ_0. A 2% offset proof stress is used to define the yield strength as the stress–strain curves do not show an obvious yield point. The specific energy W is the energy absorbed per unit initial volume of braid wall and equals the area under the nominal stress versus nominal strain curve. The $\theta_0 = 23°$ braid has a linear stress–strain response to fracture, and so the failure stress is used in the failure chart in this case.

As the braid helix angle is increased from 23° to 55°, ε_F and W increase, and E and σ_y decrease. The absorbed energy W is approximately the product of yield strength σ_y, and the final strain to failure ε_F. With increasing θ_0, ε_F increases more rapidly than σ_y decreases, and the absorbed energy, W, therefore increases with increasing θ_0. The switch in failure mechanism from fibre fracture to neck propagation occurs at about $\theta_0 = 45°$; for this transition geometry, the tows scissor in pure shear.

3. Mechanics of neck propagation in braided tubes

Steady state neck propagation occurs in braided tubes of large helix angles under uniaxial tensile loading. For example, the braid with $\theta_0 = 55°$ undergoes neck propagation with a long, constant stress plateau, as shown in *figure 3b*. A neck begins at a point of material or geometric weakness in the braid, and the nominal stress remains constant as the neck progresses along the length of the braid until the entire braid has locked-up. The neck shape is invariant as it propagates along the specimen, and the axial progress of the neck is linked directly to the axial extension imposed on the specimen. *Figure 5* shows a neck travelling along the length of a braided tube for the case of an initial helix angle of $\theta_0 = 55°$.

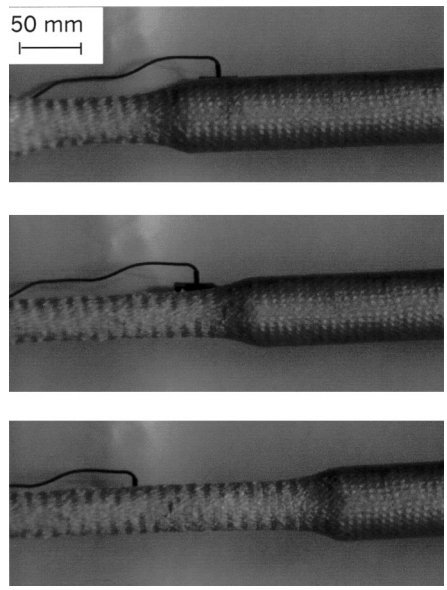

Figure 5. Video images of neck propagation along the axis of a braid under tension, for an initial helix angle $\theta_0 = 55°$.

3.1. Measured stresses in the neck

In order to construct a model for neck propagation, the local stresses within the neck are measured, as follows. The longitudinal strain in the braid and the fibre strain were monitored at mid-length of the braid using a clip gauge and a strain gauge mounted on a representative tow, respectively. The helix angle at selected points along the neck was also recorded. The membrane stresses were determined from the measured axial force on the braid and from the neck geometry. Later in this paper, we shall compare these measured stresses with the membrane stresses predicted by a micromechanical model of braid deformation.

The neck of the braided tube is treated as a doubly curved membrane with two radii of curvature, R_1 and R_2, and subjected to a longitudinal stress σ_1 and a hoop stress σ_2, as shown in *figure 6a*. Equilibrium dictates that:

$$\frac{\sigma_1}{R_1} + \frac{\sigma_2}{R_2} = \Delta p = 0, \tag{1}$$

where the pressure differential Δp across the mid-plane of the braid vanishes. Axial force equilibrium dictates that σ_1 is related to the applied axial load F by:

$$F = \sigma_1 2\pi R_2 t \cos\beta, \tag{2}$$

where β is the angle the braid makes with the axial direction, and t is the thickness of the braid as shown in *figure 6a*. The thickness of the braid does not change significantly with braid angle. The stress state can be found from the applied load via relations (1) and (2), once R_1 and R_2 have been measured along the neck. Outside the necked region the stress state is uniaxial tension. At the transition between the un-necked region and the neck, a sharp corner exists wherein bending stresses cannot be neglected. The true axial membrane stress σ_1 and true hoop stress σ_2 are shown in *figure 6b* as a function of helix angle within the neck, for the case $\theta_0 = 55°$. As the angle approaches the lock-up angle, the axial stress downstream of the neck approaches the remote stress and the hoop stress approaches zero. Selected values of R_1, R_2, β, σ_1, and σ_2 are given in *table II* as a function of helix angle θ within the neck.

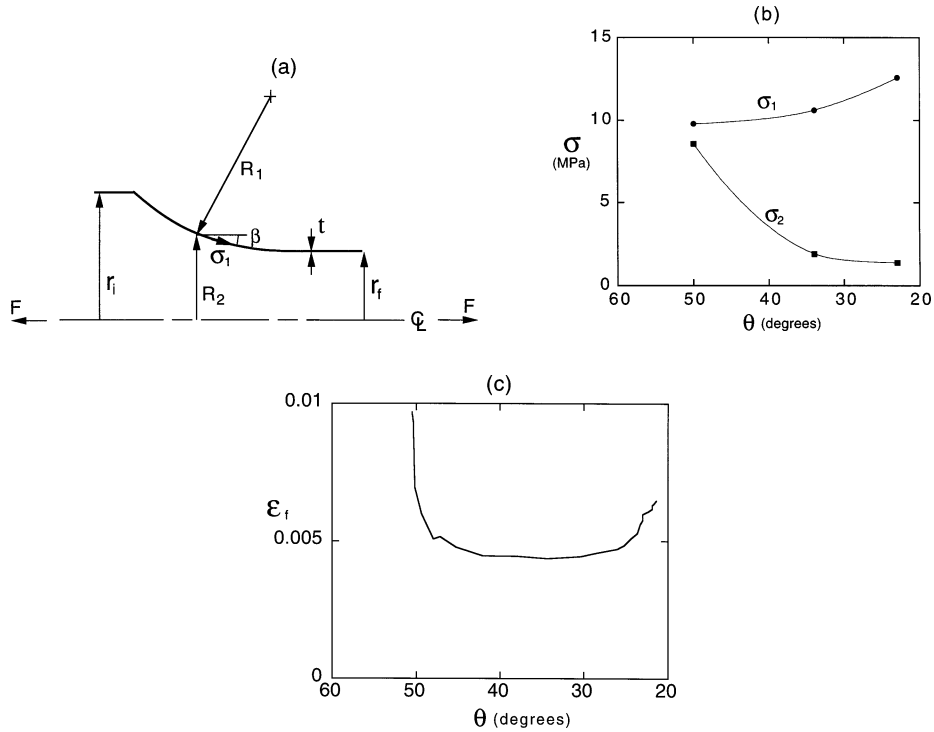

Figure 6. (a) Assumed geometry of the neck in the braided tube; (b) The measured longitudinal component σ_1 and hoop component σ_2 of Cauchy stress within the neck, for $\theta_0 = 55°$; (c) Measured fibre strain ε_f within the neck. As the neck advances, the helix angle θ decreases from the initial value $\theta_0 = 55°$.

Table II. Selected values used in the calculation of membrane stress.

Helix angle θ	Radii of neck (mm) R_1	R_2	Neck angle β	Membrane stresses (MPa) σ_1	σ_2
50°	29	25.4	38°	9.79	8.57
34°	104	18.9	12°	10.62	1.92
23°	141	15.6	5°	12.57	1.39

3.2. Resolution of measured stresses in the local fibre axes

In order to develop a micromechanical model of deformation with the neck, the stresses within each layer are measured upon treating the braid as a $\pm\theta$ laminate. Consider the typical stress state in the $+\theta$ layer, as shown in *figure 7a*. Symmetry of the $\pm\theta$ laminate dictates that the axial stress component σ_1 and the hoop stress component σ_2 equals that for the overall braid, as reported in *figure 6b*. Additionally, the $+\theta$ layer is subjected to a shear stress $\sigma_{12} = \tau_{\text{ply}}$ and the $-\theta$ layer is subjected to a shear stress $\sigma_{12} = -\tau_{\text{ply}}$, in the Cartesian reference frame (x_1, x_2) defined in *figure 7a*. The shear stress τ_{ply} is deduced from the measured in-plane stresses (σ_1, σ_2) on the braid and from the measured strain along the $+\theta$ direction, as follows.

The direct strain ε_f along the local fibre direction in a $+\theta$ layer is measured using a strain gauge adhered to a tow, prior to curing; a typical measurement is reported in *figure 6c*, for a braid of initial helix angle $\theta_0 = 55°$. We note an initial sharp spike in the fibre strain due to bending at the corner at the start of the neck. Once the

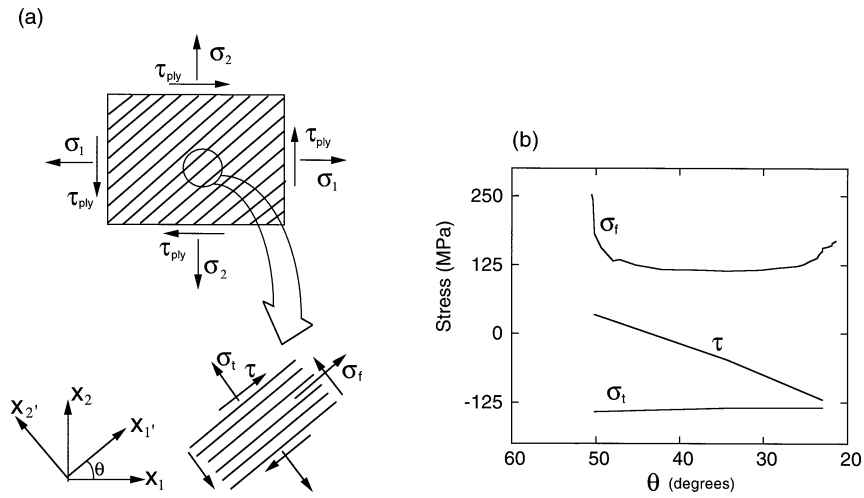

Figure 7. (a) The stress state within the $+\theta$ layer of the braid; (b) The measured stress σ_t transverse to the $+\theta$ fibres, the shear stress τ along the $+\theta$ fibre direction, and the stress σ_f in the $+\theta$ fibre direction, within the neck of a $\theta_0 = 55°$ braid.

material has entered the neck, the strain ε_f relaxes to a constant level until the braid locks-up and the strain increases sharply again. The longitudinal stress σ_f along the fibre direction in the $+\theta$ layer of the braid is estimated from a rule of mixtures calculation of the modulus of the layer in the fibre direction.

Upon rotating axes from the axial direction to the $+\theta$ direction, the components of stress in a $+\theta$ layer are given by

$$\sigma_f = \sigma_1 \cos^2\theta + \sigma_2 \sin^2\theta + \tau_{ply} \sin 2\theta, \tag{3a}$$

$$\sigma_t = \sigma_1 \sin^2\theta + \sigma_2 \cos^2\theta - \tau_{ply} \sin 2\theta, \tag{3b}$$

and

$$\tau = \frac{1}{2}(\sigma_2 - \sigma_1) \sin 2\theta + \tau_{ply} \cos 2\theta, \tag{3c}$$

where σ_t and τ are the stress transverse to the fibre direction and the shear stress along the fibre direction, respectively. Equations (3a–c) are used to deduce τ_{ply}, σ_t and τ throughout the neck from the measured values of σ_1, σ_2 and σ_f. The inferred distribution of $(\sigma_f, \sigma_t, \tau)$ within the neck is plotted in *figure 7b*. We note that the transverse stress σ_t remains compressive within the neck although we shall see below that the kinematics of deformation imply that the transverse strain is initially tensile. A micromechanical model for the stress state within the neck is developed in the following section and its predictions are compared with the experimental values.

4. Simple micromechanical models for the tensile behaviour of braided tubes

4.1. Prediction of elastic modulus

Laminate plate theory (LPT) is commonly used to predict the stiffness of fibre laminates from the elastic properties of individual laminae; it is based on the assumption that the strain state does not vary in the through-thickness direction. In the present study, laminate plate theory is used to predict the axial modulus of the braids by treating them as $\pm\theta$ laminates. The predicted elastic moduli are compared with the measured values in

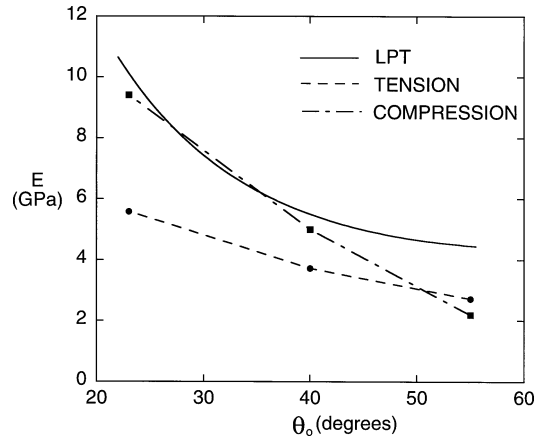

Figure 8. The axial elastic modulus E versus the initial helix angle θ_0. Values of E from laminate plate theory (LPT), and from the tensile and compressive tests are shown for $\theta_0 = 23°$, $40°$, and $55°$. The compression results are taken from (Harte and Fleck, 1999). Results are omitted for $\theta = 45°$ as a clip gauge was not used in these tests for the measurement of E.

tension and compression in *figure 8*. (The compression results were taken from (Harte and Fleck, 1999).) The experimental and theoretical values of axial elastic modulus are in good agreement, to within material scatter.

4.2. Braid kinematics

The regular braids of this study are comprised of two sets of helical tows winding in opposite directions around a cylinder. As a braid is pulled in tension, the tows scissor like the slats of a garden trellis; the helix angle decreases, and the tube increases in length and decreases in diameter. The tows continue to scissor until they become tightly packed and the braid locks-up at a helix angle θ_L.

Post-failure microscopy of the glass/epoxy braids reveals that the pattern of microcracking within the matrix between the tows is accompanied on a smaller scale by microcracking of the matrix between individual fibres of each tow. This suggests that the kinematic description of scissoring of the tows also describes the relative motion of fibres within each tow. In the following analysis, we shall smear out the fibres and matrix, and define overall stress and strain measures for the smeared-out continuum in terms of the helix angle θ.

It is convenient to calculate the strain rate within the braid using rotating orthonormal axes $(x_{1'}, x_{2'})$, with the $x_{1'}$-direction aligned with the fibres of orientation θ as shown in *figure 9*. The fibres in both the θ and the $-\theta$ directions are assumed to be inextensional; thus, in the $(x_{1'}, x_{2'})$ reference frame we have $\dot{\varepsilon}_{1'1'} = 0$ and the strain rate components of interest are the strain rate transverse to the fibres $\dot{e}_t \equiv \dot{e}_{2'2'}$ and the shear strain rate $\dot{\gamma} = 2\dot{\varepsilon}_{1'2'}$ along the fibre direction. In order to define $(\dot{e}_t, \dot{\gamma})$ we consider the relative velocities of neighbouring fibres. The true transverse strain rate $\dot{e}_t$ is given by the separation velocity of the centre-lines of two neighbouring fibres along the $x_{2'}$-direction divided by their current separation,

$$\dot{e}_t = \frac{2}{\tan 2\theta}\,\dot{\theta}. \tag{4a}$$

The shear strain rate $\dot{\gamma}$ is defined by the rate of scissoring $2\dot{\theta}$ of fibres in the θ and the $-\theta$ directions, such that

$$\dot{\gamma} = 2\dot{\varepsilon}_{1'2'} = -2\dot{\theta}. \tag{4b}$$

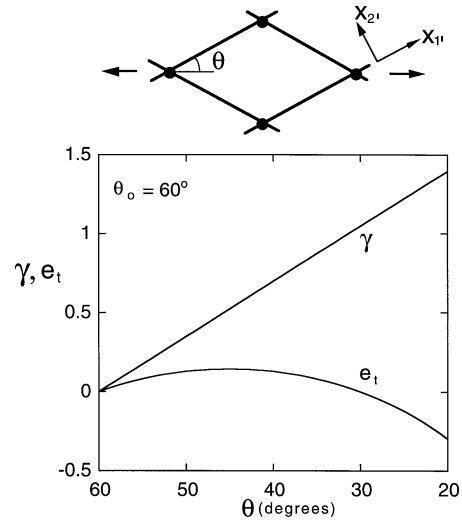

Figure 9. The predicted transverse strain e_t and shear strain γ within the braid, for an initial helix angle $\theta_0 = 60°$.

Integration of $\dot{\gamma}$ and $\dot{e}_t$ from an initial helix angle θ_0 to a current angle θ gives

$$\gamma = 2(\theta_0 - \theta) \tag{5a}$$

and

$$e_t = \ln\left(\frac{\sin 2\theta}{\sin 2\theta_0}\right). \tag{5b}$$

The transverse and shear strains are sketched in *figure 9* for the case $\theta_0 = 60°$: the shear strain increases with decreasing helix angle θ whereas the transverse strain e_t reaches a maximum at $\theta = 45°$, then drops to negative values with decreasing θ. The negative transverse strains are associated with crumbling of the matrix. For an initial helix angle $\theta_0 > 45°$ the matrix shears and initially dilates under axial extension; the distance between neighbouring fibres reaches a maximum at $\theta_0 = 45°$, at which point the matrix deforms in pure shear. For $\theta_0 < 45°$ the matrix shears and compacts under axial extension.

The axial strain of the braid ε_a is related to the current braid angle θ and to the initial braid angle θ_0 by

$$\varepsilon_a = \frac{\cos\theta - \cos\theta_0}{\cos\theta_0}, \tag{6}$$

where $2\cos\theta_0$ is the initial axial length of a braid unit cell and $2\cos\theta$ is the current length.

5. A constitutive law for the braid within the neck

A constitutive law for the braided material must be found in order to predict the plastic dissipation during neck propagation; an energy balance condition can then be used to predict the axial load for steady state neck propagation.

Figure 10a shows three scanning electron microscope (SEM) images of the state of the matrix within a typical neck; it shows that the matrix between the fibres breaks up into arrays of parallel microcracks with

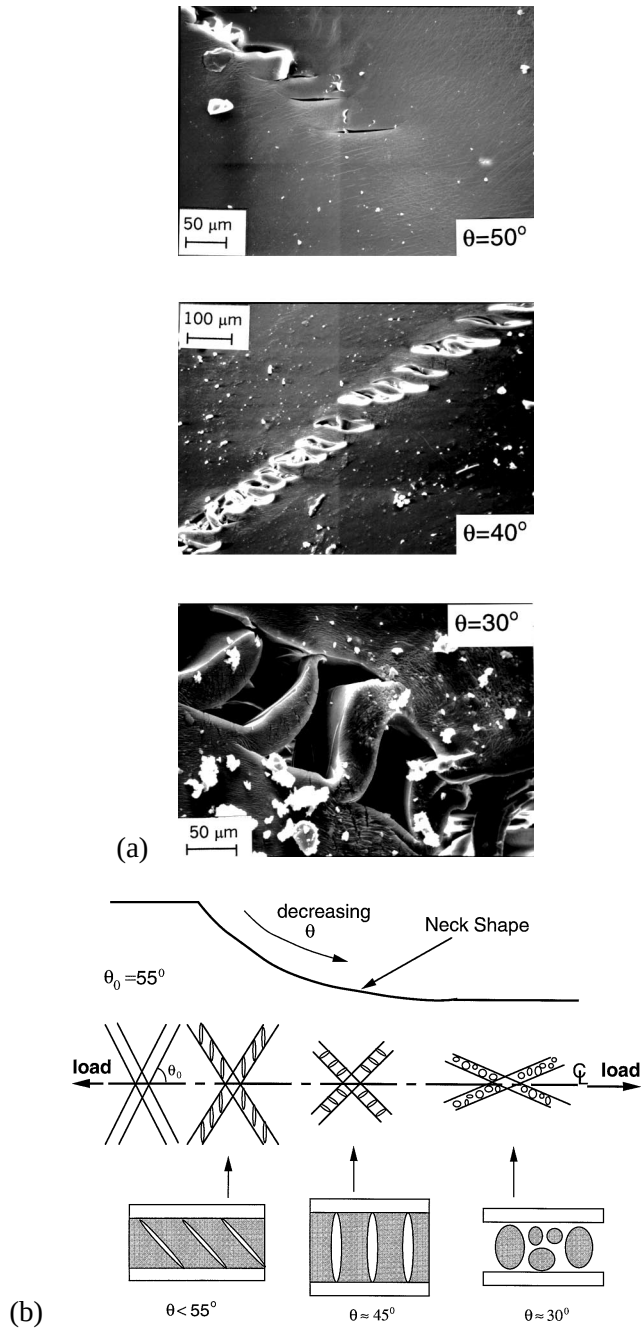

Figure 10. (a) Scanning electron microscope (SEM) images of the crack state within the neck, for the case $\theta_0 = 55°$; (b) Schematic of the neck in the braid showing the damage evolution with decreasing θ. The matrix disintegrates into an array of stubby beams, and the beams rotate as the fibres scissor.

intervening short, stubby beams. The damage sequence is sketched in *figure 10b*. Arrays of tensile microcracks form approximately perpendicular to the local loading direction. With continued loading, the fibres scissor and the beam-like ligaments within the matrix rotate until eventually they align perpendicular to the fibres. At larger strains the beams fracture and the matrix becomes rubble.

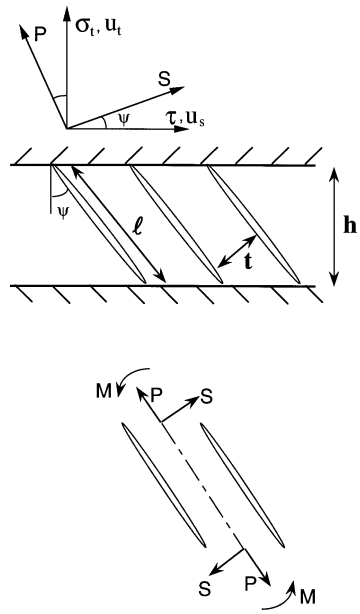

Figure 11. Representation of the matrix as an array of stubby beams of length ℓ and thickness t between fibres of spacing h, inclined with respect to the fibres at an angle ψ. Each beam is subjected to an axial load P, a shear load S and a moment M per unit thickness into the page.

The damaged matrix is modelled as a series of stubby beams using the yield surface for a rigid, ideally plastic beam subjected to end moments and a longitudinal load (Green, 1954a, b). The predicted transverse and shear stresses are then compared with the measured stresses determined from the previous section. The elastic deformation is small and can be neglected.

5.1. The yield surface

The damaged matrix is treated as a series of stubby beams of length ℓ and thickness t made from rigid, ideally plastic material, see *figure 11*. The beams are subjected to both an axial force P and a moment M per unit depth, upon resolving the macroscopic traction due to the shear stress τ and transverse stress σ_t as defined in equations (3a–c). Green (1954a, b) has shown that the collapse locus for P and M for stubby beams is adequately represented by that for a long thin beam:

$$\Phi(M, P) = \left(\frac{P}{P_0}\right)^2 \pm \left(\frac{M}{M_0}\right) - 1 = 0, \tag{7}$$

where $P_0 = 2kt$, $M = S\ell/2$ and $M_0 = t^2k/2$. Here, k is the shear yield strength of the matrix and S is the resultant shear force, as shown in *figure 11*. Force resolution gives

$$S = (\tau \cos\psi + \sigma_t \sin\psi)\frac{t}{\cos\psi} \tag{8a}$$

and

$$P = (-\tau \sin\psi + \sigma_t \cos\psi)\frac{t}{\cos\psi}, \tag{8b}$$

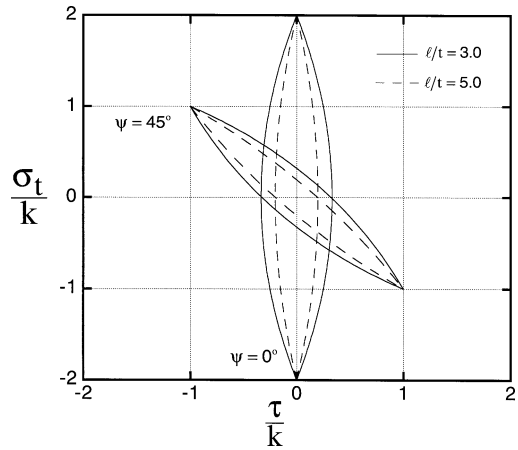

Figure 12. The yield surface of the matrix beams in axes of transverse stress σ_t and shear stress τ. As the fibres scissor, the beams rotate, and the yield surface rotates in stress space.

where the crack angle ψ is defined in *figure 11*. The yield locus (7) can then be rewritten as

$$\Phi(\tau, \sigma_t) = \frac{1}{\cos\psi}\,\frac{\ell}{t}\left(\frac{\tau}{k}\cos\psi + \frac{\sigma_t}{k}\sin\psi\right) + \frac{1}{4}\,\frac{1}{\cos^2\psi}\left(-\frac{\tau}{k}\sin\psi + \frac{\sigma_t}{k}\cos\psi\right)^2 - 1 = 0. \tag{9}$$

Note that the cracks have an initial angle ψ_0 and rotate to an orientation perpendicular to the fibres ($\psi = 0°$). The yield surfaces for $\psi = 0°$ and $\psi = 45°$ simplify to:

$$\Phi = \frac{\ell}{t}\,\frac{\tau}{k} + \frac{1}{4}\left(\frac{\sigma_t}{k}\right)^2 - 1 = 0 \quad \text{for } \psi = 0° \tag{10a}$$

and

$$\Phi = \frac{\ell}{t}\left(\frac{\tau}{k} + \frac{\sigma_t}{k}\right) + \frac{1}{4}\left(-\frac{\tau}{k} + \frac{\sigma_t}{k}\right)^2 - 1 = 0 \quad \text{for } \psi = 45° \tag{10b}$$

and are plotted in *figure 12* for selected values of ℓ/t and ψ. In subsequent calculations we shall take $\ell/t = 3$ to correspond to the value observed from the SEM images of the neck. A feature of the yield surface is the pronounced vertex at each end. At these vertices the strain rate can be in any direction within the forward cone of normals, implying that the stress state is usually at a vertex.

5.2. Kinematics of matrix deformation

To proceed, an expression is obtained for the motion of the matrix beams as the braid deforms. The relationship between the velocity of the fibres tangential to the fibre direction and perpendicular to the fibre direction, $\dot{u}_s$ and $\dot{u}_t$, and the strain rates, $\dot{\gamma}$ and $\dot{e}_t$, in the composite is given by:

$$\frac{\dot{u}_s}{h} = \frac{\dot{\gamma}}{1 - V_f} \tag{11}$$

and

$$\frac{\dot{u}_t}{h} = \frac{\dot{e}_t}{1 - V_f}, \tag{12}$$

where h is the distance between fibres and V_f is the fibre volume fraction. Here, u_s us is the tangential relative displacement of two fibres and u_t is the normal relative displacement of two fibres, as shown in *figure 11*.

The rotation rate $\dot{\psi}$ is related to the beam motion by:

$$-\dot{\psi} = \frac{1}{\ell}(\dot{u}_s \cos\psi + \dot{u}_t \sin\psi). \tag{13}$$

Upon substituting (11) and (12) into (13) and making use of the connection $h = \ell \cos\psi$, the rate of change of the crack inclination $\dot{\psi}$ is related to the strain rate $\dot{e}_t$ and $\dot{\gamma}$ by

$$\dot{\psi} = -\frac{\cos^2\psi}{1 - V_f}\,\dot{\gamma} - \frac{\cos\psi \sin\psi}{1 - V_f}\,\dot{e}_t. \tag{14}$$

Recall that the shear and normal strain rate, $\dot{\gamma}$ and $\dot{e}_t$, have already been related to the helix angle rate $\dot{\theta}$ by equations (4a) and (4b).

5.3. The associated flow rule

Associated plastic flow is assumed such that the plastic strain rate $\dot{\varepsilon}_{ij}$ is given by

$$\dot{\varepsilon}_{ij} = \frac{1}{H}\frac{\partial \Phi}{\partial \sigma_{ij}}\frac{\partial \Phi}{\partial \sigma_{kl}}\dot{\sigma}_{kl}, \tag{15}$$

where the overall hardening modulus H remains to be specified. Recall that the underlying matrix material is taken as rigid, ideally plastic and so the hardening modulus H is associated with the geometric hardening accompanying beam rotation, and not due to intrinsic material strengthening. The strain rates can be specified by the shear strain rate and the strain rate normal to the fibres $\dot{e}_t$ such that

$$\dot{\gamma} = \frac{1}{H}\frac{\partial \Phi}{\partial \tau}\left(\frac{\partial \Phi}{\partial \tau}\dot{\tau} + \frac{\partial \Phi}{\partial \sigma_t}\dot{\sigma}_t\right) \tag{16a}$$

and

$$\dot{e}_t = \frac{1}{H}\frac{\partial \Phi}{\partial \sigma_t}\left(\frac{\partial \Phi}{\partial \tau}\dot{\tau} + \frac{\partial \Phi}{\partial \sigma_t}\dot{\sigma}_t\right). \tag{16b}$$

The consistency relation for continued plastic yielding reads

$$\dot{\Phi} = \frac{\partial \Phi}{\partial \tau}\dot{\tau} + \frac{\partial \Phi}{\partial \sigma_t}\dot{\sigma}_t + \frac{\partial \Phi}{\partial \psi}\dot{\psi} = 0. \tag{17}$$

From equations (16) and (17) and the kinematical relation (13), the strain rate can be rewritten as:

$$\dot{\gamma} = \frac{1}{H}\frac{\partial \Phi}{\partial \tau}\frac{\partial \Phi}{\partial \psi}\frac{h}{\ell(1 - V_f)}(\dot{\gamma}\cos\psi + \dot{e}_t \sin\psi), \tag{18a}$$

$$\dot{e}_n = \frac{1}{H}\frac{\partial \Phi}{\partial \sigma_t}\frac{\partial \Phi}{\partial \psi}\frac{h}{\ell(1 - V_f)}(\dot{\gamma}\cos\psi + \dot{e}_t \sin\psi) \tag{18b}$$

and the hardening modulus H follows by eliminating $\dot{\gamma}$ and $\dot{e}_t$ from the two simultaneous equation (18a and b) to give

$$H^{-1} = \left(\frac{\partial \Phi}{\partial \tau} \cos\psi + \frac{\partial \Phi}{\partial \sigma_t} \sin\psi \right) \frac{\partial \Phi}{\partial \psi} \frac{\cos\psi}{1 - V_f}. \tag{19}$$

We now have a complete formulation for each layer of the composite. The yield function Φ is a function of the variables, τ, σ_t, k, and ψ. From the flow rule (15) and the consistency relation (17) the strain rates $\dot{\gamma}$ and $\dot{e}_t$ are known. The kinematical relation (14) provides $\dot{\psi}$ in terms of $\dot{\gamma}$ and $\dot{e}_t$.

6. Comparison of predicted and measured stress state in the neck

The equations developed above provide a constitutive description for the braid. Due to the shape of the yield surface the stress is at a vertex of the yield surface unless $|\dot{u}_t/\dot{u}_s|$ is close to zero. At each vertex we have $M = 0$ and $|P| = 2kt$. The normal and shear stresses then simplify to:

$$\frac{\tau}{k} = 2 \sin\psi \cos\psi \tag{20a}$$

and

$$\frac{\sigma_t}{k} = -2 \cos^2\psi. \tag{20b}$$

The current beam orientation is given by $\psi = \psi_0 + 2\Delta\theta$ where $\Delta\theta \equiv \theta - \theta_0$, resulting in

$$\frac{\tau}{k} = 2 \sin(\psi_0 + 2\Delta\theta) \cos(\psi_0 + 2\Delta\theta) \tag{21a}$$

and

$$\frac{\sigma_t}{k} = -2 \cos^2(\psi_0 + 2\Delta\theta). \tag{21b}$$

Figure 13 gives a comparison of the predicted values of (τ, σ_t) within the neck and the measured values from the membrane analysis of Section 3.2. The trends of the predicted values are in rough agreement with

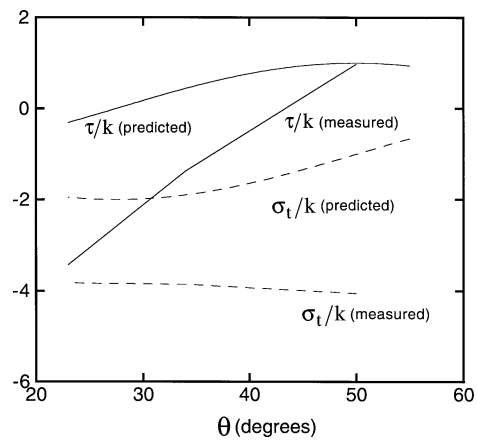

Figure 13. The predicted and measured stress within the neck, resolved along the fibre direction, for the case $\theta_0 = 55°$.

the measured values. The largest discrepancies in shear stress occurs at small values of the helix angle θ. At these helix angles the matrix exists as rubble rather than as an array of stubby beams and the constitutive model developed above is no longer applicable.

6.1. Prediction of the neck propagation stress

In general, a Maxwell-type energy construction cannot be used to predict the applied load for the propagation of an instability, such as a neck, within a flow theory solid. However, in the present case, the deformation state within the neck of the braid is governed by the single degree of freedom, θ, and thus the loading path in stress state is known. An energy balance method can then be used in order to estimate the propagation stress.

The internal energy dissipated in scissoring the fibres from $\theta = \theta_0$ to a final angle $\theta = \theta_L$ is

$$W = V_0 \int_0^{\gamma_L} \left[\tau \frac{V}{V_0}\right] \mathrm{d}\gamma + V_0 \int_0^{e_t^L} \left[\sigma_t \frac{V}{V_0}\right] \mathrm{d}e_t, \tag{22}$$

where $\gamma_L \equiv \gamma(\theta = \theta_L)$ and $e_t^L \equiv e_t(\theta = \theta_L)$ are given by (5), and τ and σ_t are the macroscopic shear stress and transverse stress in the current configuration, in the local fibre axes. The ratio of current volume V to the initial volume V_0 of a braid element is given by

$$\frac{V}{V_0} = \frac{\sin 2\theta}{\sin 2\theta_0}. \tag{23}$$

Since the scissoring of the braid is dictated by a single degree of freedom θ we can re-write (22) as

$$W = V_0 \int_{\theta_0}^{\theta_L} \left[-\tau \frac{2\sin 2\theta}{\sin 2\theta_0}\right] \mathrm{d}\theta + V_0 \int_{\theta_0}^{\theta_L} \left[\sigma_t \frac{2\cos 2\theta}{\sin 2\theta_0}\right] \mathrm{d}\theta \tag{24}$$

and the energy balance can be written:

$$P(L_1 - L_0) = A_0 L_0 \left\{ \int_0^{\gamma} \left[\tau \frac{\sin 2\theta}{\sin 2\theta_0}\right] \mathrm{d}\gamma + \int_0^{e_t} \left[\sigma \frac{\sin 2\theta}{\sin 2\theta_0}\right] \mathrm{d}e_t \right\}. \tag{25}$$

The left-hand side of the equation represents the energy contribution of the applied load, P in changing the length of a section from L_0 to L_1; the final length L_1 is given by $L_0\varepsilon_a$, where the axial strain ε_a, as defined in (6), is evaluated at $\theta = \theta_L$. The right-hand side is the energy per unit initial volume due to material deformation, multiplied by the original volume of the wall of the tube A_0L_0. The above integral has been evaluated for braids with initial helix angles in the range $\theta_0 = 60°$ to $\theta_0 = 45°$, using relations (21a and b) for τ and σ_t and (5a and b) for γ and e_t. (For angles θ_0 less than 45° neck propagation does not occur.)

The predicted propagation load P, energy absorption per unit volume W, and final axial strain ε_a are plotted in *figure 14* for an assumed lock-up helix angle $\theta_L = 21°$. The trends are as expected: the energy absorbed and the final axial strain increase with increasing initial helix angle and the propagation load decreases. The predictions may be compared with the measured propagation load for the case $\theta = 55°$ and $\theta_L = 21°$. In the experiment, the initial wall cross-sectional area was 200 mm^2, and the shear strength of the epoxy was 22 MPa from a uniaxial tensile test on a $\pm 45°$ braid (see *figure 3*). The predicted propagation load, 9.9 kN, is approximately twice the measured value of 4.0 kN. The discrepancy is not surprising considering the limited accuracy of the beam model for the cracked matrix. Similar agreement is noted for the absorbed energy W, but good agreement is found between the final axial strain of 0.60, given by equation (6) and the observed lock-up strain of 0.62.

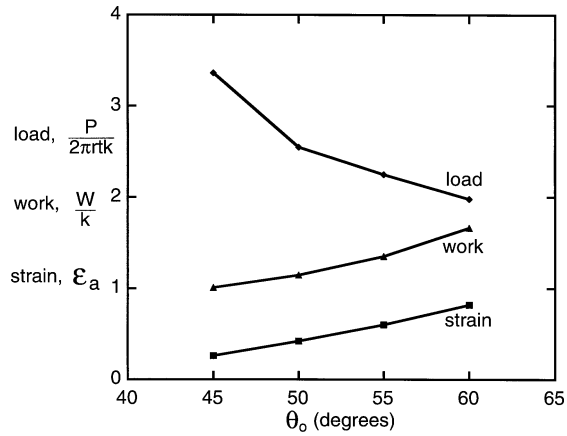

Figure 14. The normalised propagation load $P/2\pi rtk$, normalised energy absorption per unit volume W/k and the final axial strain ε_a for neck propagation as a function of the initial helix angle θ_0. $\theta_L = 21°$.

7. Concluding remarks

Tubular braids fail in tension by fibre failure for small initial helix angles and by neck propagation for large initial helix angles. The switch in failure mode from fibre failure to neck propagation is accompanied by a large increase in energy absorption and strain to failure but by a large drop in yield strength.

Attention has been focused on the case of an initial braid angle θ_0 greater than 45°. The stress state in the neck is deduced from the observed neck shape using a membrane analysis and from strain gauges impregnated in the braid prior to epoxy infiltration. A micromechanical model has been developed of the deformation state within the neck. The predicted propagation stress increases, whereas the strain to lock-up and the absorbed energy decrease with increasing helix angle, in agreement with the trends observed experimentally. The limited results of the current study suggest that braided composites have potential as practical energy absorbers: they deform in tension at almost constant stress over large extensional strains.

Acknowledgements

The authors wish to thank the Natural Sciences and Engineering Research Council of Canada, the Newton Trust, and ONR through the grant number N0014-91-J-1916 for their financial support and Cambridge Consultants Ltd for the provision of test materials.

References

Chater E., Hutchinson J.W., 1984a. On the propagation of bulges and buckles. J. Appl. Mech. 51, 269–277.

Chater E., Hutchinson J.W., 1984b. Mechanical analogs of coexistent phases. In: Phase Transformations and Material Instability in Solids, Academic Press, Inc., pp. 21–36.

Chou T.-W., 1992. Microstructural Design of Fiber Composites. Cambridge Solid State Science Series, Cambridge University Press.

Green A.P., 1954a. A theory of the plastic yielding due to bending of cantilevers and fixed-ended beams. Part 1. J. Mech. Phys. Solids 8, 1–15.

Green A.P., 1954b. A theory of the plastic yielding due to bending of cantilevers and beams. Part II. J. Mech. Phys. Solids 8, 143–155.

Harte A.-M., Fleck N.A., 1999. Deformation and failure mechanisms of braided composite circular tubes in compression and torsion. Eur. J. Mech. A, to appear.

Kyriakides S., Chang Y.-C., 1990. On the inflation of a long elastic tube in the presence of axial load. Int. J. Solids Structures 26 (9/10), 975–991.

Kyriakides S., 1994. Propagating instabilities in structures. In: Advances in Applied Mechanics, Vol. 20, Academic Press, Inc., pp. 67–189.